A review of microstructural characterization and liquid transport in porous materials through image processing techniques

Dang Mao Nguyen, Jing Zhang, Mourad Rahim, Dong Quy Hoang, Geoffrey Promis, Mohammed El Ganaoui, Anh Dung Tran Le

A review of microstructural characterization and liquid transport in porous materials through image processing techniques

Dang Mao Nguyen[1]*, Jing Zhang[2], Mourad Rahim[1], DongQuy Hoang[3,4]*, Geoffrey Promis[5], Mohammed El Ganaoui[1], Anh Dung Tran-Le[5]*

[1]Université de Lorraine, LERMAB, 186 rue de Lorraine, 54400 Cosnes-et-Romain, France

[2]State Key Laboratory of Environmental Criteria and Risk Assessment, State Environmental Protection Key Laboratory for Lake Pollution Control, National Engineering Laboratory for Lake Pollution Control and Ecological Restoration, State Environmental Protection Scientific Observation and Research Station for Lake Dongtinghu (SEPSORSLD), Chinese Research Academy of Environmental Sciences, Beijing, 100012, PR China

[3]Faculty of Materials Science and Technology, University of Science, Vietnam National University, Ho Chi Minh 700000, Vietnam.

[4]Vietnam National University, Ho Chi Minh City 700000, Vietnam.

[5]Laboratoire des Technologies Innovantes, EA 3899 – Université de Picardie Jules Verne, IUT Amiens, Avenue des Facultés – Le Bailly, Amiens Cedex 1, 80025, France.

*Corresponding authors : dang.nguyen@univ-lorraine.fr (D.M. Nguyen) ; htdquy@hcmus.edu.vn (D.Q. Hoang) ; anh.dung.tran.le@u-picardie.fr (A.D. Tran-Le).

Table of content

ABSTRACT

The mechanism of fluid and heat transmission within materials with complex porous structures has not yet been fully explored and understood using basic analytical techniques. Therefore, the lack of advanced equipment and techniques has left an important knowledge gap in explaining the complex mechanisms of fluid motion and heat transfer in complex porous structures. This review provides an overview of how image analysis and processing techniques allow insight into the complex and heterogeneous porous structure of materials and explains the mechanism of heat and mass transfer in these complex porous materials in 3D and 4D observation in different directions. Accordingly, it provides interesting results related to the evaluation of microporous properties of complex porous materials including porosity, distribution and size of pores, distribution and orientation of fibers, tortuosity and mechanism of cracking and destruction of the porous materials under mechanical tests. It also explains the mechanism of liquid transport in porous materials through 3D/4D observation thanks to image processing techniques. Therefore, this review has completed some limited knowledge in microstructural analysis and helped to understand the physical phenomena of liquid transfer in complex porous materials that were not fully exploited by experimental or simulation work. The paper also provides useful data for physical model simulation of imbibition and drying porous materials.

Keywords: microstructure; image processing technique; tomography; porous materials; liquid transport in porous media.

1. Introduction

The microstructure is one of the most important properties because it directly affects their physico-chemical, mechanical, and hygrothermal properties as well as the heat and mass transfer mechanism within the porous materials. The microstructure including porosity, pore size and shape, pore surface area, and pore distribution of the materials are usually studied by experimental analysis techniques such as Brunauer-Emmett-Teller (BET), mercury intrusion porosimetry (MIP), and nuclear magnetic resonance (NMR) (Lai et al., 2018) and classic image processing methods (Arashpour et al., 2021). However, these methods have many limitations because they cannot fully describe the porous structure properties of materials such as the inability to measure closed pores or the connection between pores as well as some limitations observing the distribution of pore and reinforcement phases inside the materials. In fact, the development of image techniques such as tomography or synchrotron enables the observation of the three-dimensional (3D) structure of materials at a high resolution. Accordingly, a series of two-dimensional (2D) images obtained from tomography/synchrotron techniques was processed through image processing techniques to analyze and extract the porous characterization that was not possible with previous experimental techniques. In the literature, tomography has combined different image processing techniques to analyze a series of images obtained from this device regarding the microporous structure of different materials. Accordingly, the 3D porous structure of poplar wood was observed at a very high resolution of about 400 nanometers thanks to nanosource X-ray tomography (Perré et al., 2022). Accordingly,

the morphology and function of pits on the cell wall of wood were observed in detail to explain the physical transport phenomenon inside this wood and confirmed the proposed hypotheses. Furthermore, the porous structure of biobased composites reinforced with natural fibers has also been studied using tomography combined with Avizo and ImageJ software for image processing (Nguyen et al., 2022a). Accordingly, the porous properties including porosity, distribution, and size of pores and fibers inside the composites have been processed and reported. Similarly, the microporous characterization of various natural fiber-reinforced concrete materials has also been studied and reported in the literature (du Plessis and Boshoff, 2019; Pham et al., 2020b; Ríos et al., 2019). The morphological characteristics of aggregate concrete recycled were also investigated using digital image processing technique (Ma et al., 2021). Accordingly, the 3D observation of the pore and fibers has been processed and represented through different colors inside the materials. Moreover, the porous properties of different sandstone and carbonate samples (Safari et al., 2021) and some porous materials for geoscience applications were also investigated and reported in the literature (Luo et al., 2019; Roostaei et al., 2020; Song et al., 2019a; Song et al., 2019b) using X-ray microtomography (μCT) and scanning electron microscopy (SEM) techniques in combination with image processing techniques. In addition, combined tomography with image processing was also applied to detect microcracks and crack development mechanism inside materials through 3D observations (Flansbjer et al., 2018; Rucka et al., 2021). These results have allowed to explain the failure mechanism of materials when subjected to external forces through methods of testing mechanical

properties. The wood and bio-sourced materials are become more interesting today, especially, in the field of civil construction because of the increasing demand for sustainable buildings including hygrothermal comfort and efficiency and reduction in CO_2 emission to the environment. Many European countries have introduced regulations on increasing the content of green materials such as wood and bio-sourced materials in new constructions to reduce the environmental impact reported in many regulations. As a result, wood or wood-based materials such as cross-laminated timber (CLT) have been particularly interested in using in high quantities. In fact, at the construction site, the contact of wood materials with liquid water is inevitable. Wood is a highly hygroscopic material, the contact of wood with water causes serious problems such as swelling, structural damage, and creating a humid environment conducive to the growth of fungus and threatening the works safety. Therefore, to minimize and avoid problems arising and protect wood-based materials at construction sites, the interactions with water need to be understood first. In addition, emerging problems need to be carefully evaluated for precaution. Warnings must be given as regulations to guide construction sites to eliminate potential problems as much as possible. In fact, the interactions between water vapor and wood or wood-derived materials have been reviewed and reported for a long time (Engelund et al., 2013; Nguyen et al., 2021a; Thybring et al., 2022). The behavior, interactions, hygrothermal and durability properties of wood and bio-sourced materials with water vapor have been reported (Nguyen et al., 2018a; Nguyen et al., 2017; Promis et al., 2018; Promis et al., 2019; Rahim et al., 2017). However, so far, there is still a lack of information, actual data, or

predictive models between these materials and water (liquid or vapor phase) to guide the construction sites. Furthermore, the mechanism of liquid water penetration into wood and evaporation of water from wood and bio-sourced materials under different conditions (pressure or surface heating) has less been established and specifically reported.

This review provides detailed approaches in image processing techniques to characterize the microporous structure of porous materials including wood, concrete, and composite materials reinforced with natural fibers. Accordingly, a series of image processing methods have been synthesized and provided to fully analyze the porous properties of these materials from the shape and pores/fibers distribution to the total porosity calculation. In addition, the pores connection, the tortuosity, and the interface between the phases inside the materials are also analyzed to explain the microstructure influence on physical, physicochemical, mechanical, and other properties of the porous materials. In addition, tomography techniques combined with image processing methods are also applied to explain the mechanism of crack formation and internal destruction of the materials under the influence of external force. Finally, the movement of liquids including water and oil inside porous materials through imbibition and drying is also observed in 3D through these techniques to give new knowledge and analytical methods related to the field of physics transfer within bio-based porous materials.

2. Pore identification and characterization

2.1. A pore type classification

In the literature, pores could be divided into different types due to their diameter: micropores smaller than 1.25 nm, mesopores from 1.25 nm to 25 nm, macrospores macropores from 25 nm to 1 μm, and other large pores from 5 μm to 50 μm (Moravcová et al., 2016). They can also be divided into gel pores (1-5 nm), capillary pores (5-4000 nm), entrained air pores (1-2000 μm), and entrapped air pores (1-10 mm) according to their characteristics (Moravcová et al., 2016).

2.2. Pore geometry and characterization

Direct and indirect measurement methods have been used to acquire information on pores (Wu et al., 2019). Direct methods include the mercury injection capillary pressure method (MIP, AutoPore IV mercury porosimeter, in the range of 5 nm to 10^6 nm) (Niu et al., 2020), using air-pore analyzers like RapidAir 457 (Carlson et al., 2006), gas adsorption method using Autosorb-1-c (Zhang et al., 2017), etc. The latter normally indicates image-based techniques that can detect not only air pores but also fibers in the meantime. Image-based techniques, both 2D and 3D, will be mainly discussed in this section. Problem of this method is high pressure which can lead to damage the porous structure. Thanks to rapid advances in imaging technology, such as scanning electron microscope (SEM, 2D), X-ray computed tomography (X-CT), Nuclear Magnetic Resonance (NMR), X-ray microscope, the structure of concrete can be observed at different scales. Lim et al. (Lim et al., 2018) used SEM combined focused ion beam method to obtain 3D images of concrete, the material was iteratively milled each 10 nm and then scanned by SEM. The resolution reached up to 10 nm, therefore, not only the porosity, and pore diameter but also the

capillary pores and the gel pores could be detected. Micro-computed tomography (μ-CT) is one of the most popular methods to visualize concrete, and the specimen can be reconstructed by associate software such as Avizo (Nguyen et al., 2021a), Volume Graphics VGSTUDIO MAX (Borges de Oliveira et al., 2016; du Plessis and Boshoff, 2019), TXM Reconstructor (Bacaicoa et al., 2017), Amira ZIB Edition (Trofimov et al., 2018), etc. Once the 2D/3D image of the specimen is obtained, various image processing methods such as Avizo, ImageJ, coding software such as MATLAB, Python, C++, a combination of these, etc. can be applied to obtain more information (Nguyen et al., 2021a). The image processing procedure is similar to that in other fields of life and medical science. Normally, these commercial software programs work well, are more friendly, and are easier for operators to use, but their algorithm is unknown, which can lead to confusion, especially in rigid research areas. For ImageJ, a great deal of research and testing must be done to select an appropriate package, users need to code themselves in the non-standard case, and a reputable operation needs to be performed when too many datasets exist. Nevertheless, ImageJ is a convenient open-source software and has a huge package. Practically, in-house codes, written by MATLAB, Python, C++, or other software, are more useful and can satisfy those special cases and each procedure is clear. Those programs are written in a laboratory and are used for future researchers, therefore, continuous work in a laboratory shows their own advantages. To conclude, users should choose the appropriate methods according to their own situation. Bordelon et al. (Bordelon et al., 2020)

193 detailed the image processing method for pores and fibers detection, which may be useful
194 for beginners who want to understand or use the image processing method.
195 Pore size distribution, porosity, and the fractal dimension of the pore surface are three
196 crucial parameters to express pore characteristics. The pore size distribution has been
197 studied in both 2D and 3D, and pixel (or voxel) number counting is the most convenient
198 size measurement method. 2D pore size distribution could be obtained by the average of
199 10 Feret diameters and 3D pore size distribution by the average equivalent diameter of
200 pores as regarded as spheres (Wen et al., 2020; Yuan et al., 2018). Considering the real
201 feature of pores in the concrete, which is no-spherical, the chord-length distribution was
202 also used to describe the pore size distribution (Pandit and Ranade, 2016). Lately, Chung
203 et al. (Chung et al., 2020) reported that the chord-length distribution was closer to the result
204 using the conventional method of RapidAir than the volume-based pore diameter
205 distribution. Wen et al. (Wen et al., 2020) used ImageJ to analyze 2D images (Figure 1 top-
206 right) and Avizo to analyze 3D images (Figure 1 top-center) which were obtained by μ-CT
207 and reconstructed by the associate software Avizo. The 2D pore size was calculated by the
208 average of 10 Feret diameters of all the 720 slices and the 3D equivalent diameter was
209 generated from pores volume considering the pores as a sphere (Figure 1 bottom). Wen et
210 al. (Wen et al., 2020) reported that the pore size ranged from 0 to 15 mm in 3D analysis,
211 while the pore size ranged from 0 to 45 mm in 2D analysis and that the pore size obeyed a
212 normal distribution with a large number of small pores, regardless of the size of the
213 concrete aggregates both in 2D and 3D analysis.

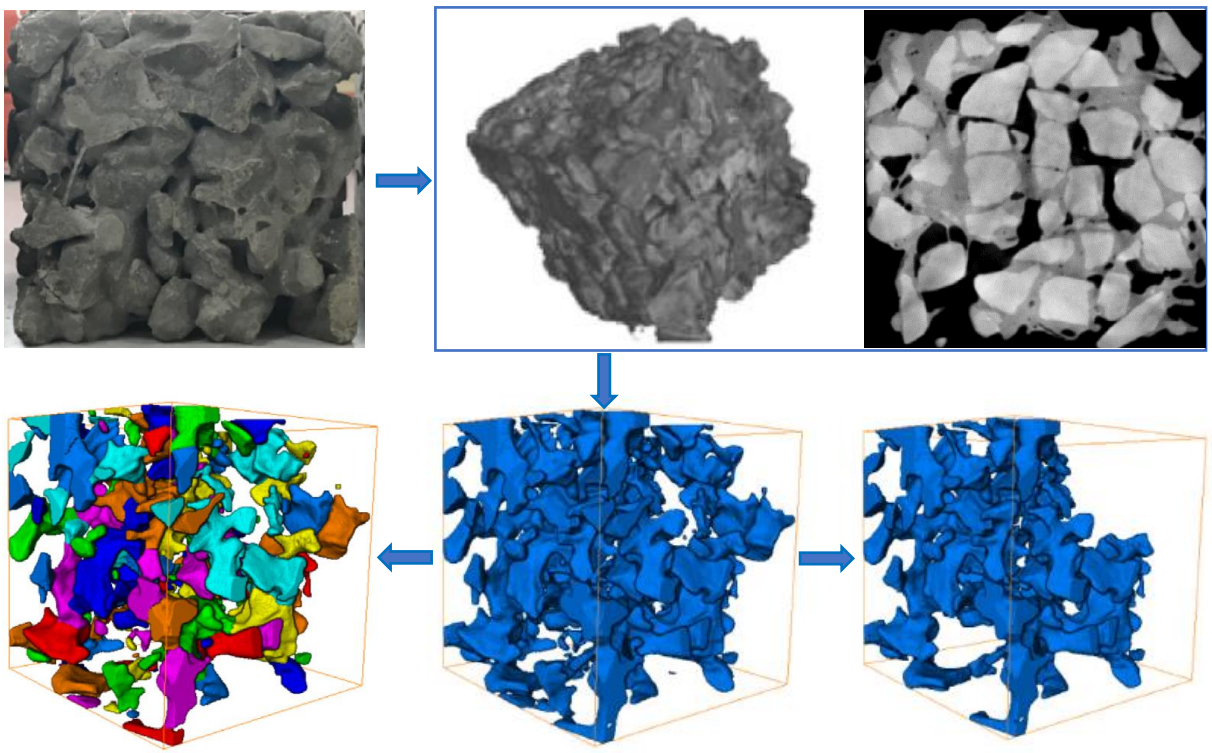

Figure 1 Specimen (top-left), 3D images reconstructed by Avizo (top-center) and 2D slice of specimen treated by ImageJ (top-right) based on the scanning data from μ-CT, pores of the specimen generated by the image processing function of Avizo (bottom-center), pores colored according to their sizes (bottom-left), and the connected pores (bottom-right) (Wen et al., 2020). The specimen size is $(100\ mm)^3$.

Porosity can be obtained by setting the spherical and size parameters empirically, as shown in Figure 2: the left image displays a slice of the μ-CT image of concrete, then segmentation was performed by the threshold, and finally, the porosity was generated based on spherical (sphericity > 0.6 and diameter > 60 μm) or non-spherical pores (sphericity < 0.6) (du Plessis and Boshoff, 2019). The porosity generated from 2D and 3D images got the same value and no difference from the experimental value, which was obtained by Archimedes'

principle-based method performed by immersing the concrete in water (Wen et al., 2020). Based on pores volume separated by pore throats, Yu et al. (Yu et al., 2019) found that pores are more like an ellipse and express the shape of pores by the number from 1 to 6, which was calculated using the major axis divided by the minor axis to express how close the pores to a circle. Zhang et al. (Zhang et al., 2018) and Yu et al. (Yu et al., 2019) obtained the porosity by the average pores area of about 20 slices of 2D CT images divided by the slice area and no significant difference were found comparing to the porosity from 3D images. The 3D connected porosity was logically lower than the actual porosity obtained by the displacement of water test (Zhang et al., 2018). The porosity had a higher value at the center of the concrete than at the top and bottom and the pore size increased along the porosity (Zhang et al., 2018).

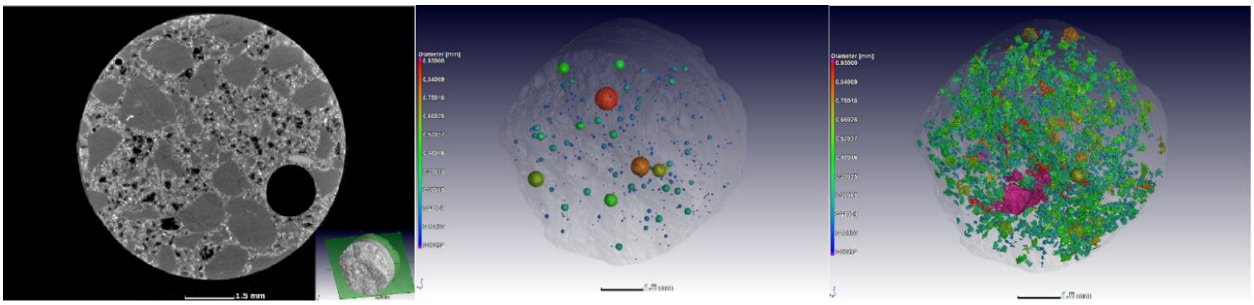

Figure 2 Porosity of concrete sample. CT slice image (left), the largest spherical (center) and non-spherical pores (right). The colors in the middle and right images represented the different diameters of pores, scale bar, 0.15 mm (du Plessis and Boshoff, 2019).

Ríos et al. (Ríos et al., 2019) reported a reduced porosity and an increased pore size due to the addition of fibers and they could also be affected by the characteristics of fibers (Figure

3). Additionally, the average sphericity which was defined as $\pi^{1/3} \times \left(6V_{pore}\right)^{2/3}/A_{pore}$, where V_{pore} and A_{pore} represents the pore volume and surface area respectively, reduced with the presence of fibers. The shape of pores showed a tendency from spherical to oval with fibers due to the distortion of the matrix (Ríos et al., 2019). Simões et al (Simões et al., 2017) specifically compared the concrete containing three different fibers of polypropylene, glass, and steel with dosages of 0.5%, 1%, 1.5%, and 2%, respectively. The porosity of the concrete containing the polypropylene fibers increased over the fibers content, while it showed a slight decrease in the case of glass. In the case of steel fibers, the porosity had a slightly decreased along the content up to 1.5%, however, it increased at the content of 2%. Thus, the porosity of fiber-reinforced concrete needs to be observed specifically and no general conclusion can be conducted. Additionally, the concrete manufacturing method also affects the porosity. In addition, the porous properties including pore size, porosity, and pore distribution of biodegradable composite from PLA/PEG reinforced by bamboo fibers and powders were investigated by using tomography and Avizo software for image processing, as presented in Figure 4.

(a) (b) (c) (d)

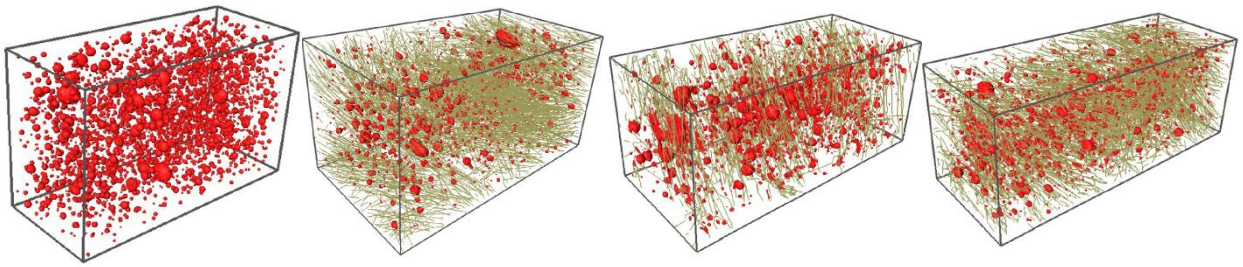

Figure 3 : Pores distribution in the concrete contains different kinds of fibers (Ríos et al., 2019). (a) no fibers, (b) micro-fibers, straight OL 13/.20, 13 mm in length and 0.20 mm

in diameter, (c) macro-fibers, hooked end Dramix RC80/30CP, 30 mm in length and 0.38 mm in diameter, and (d) mixture of 50% micro- and 50% macro-fibers. The red and gold represent the pores and fibers, respectively.

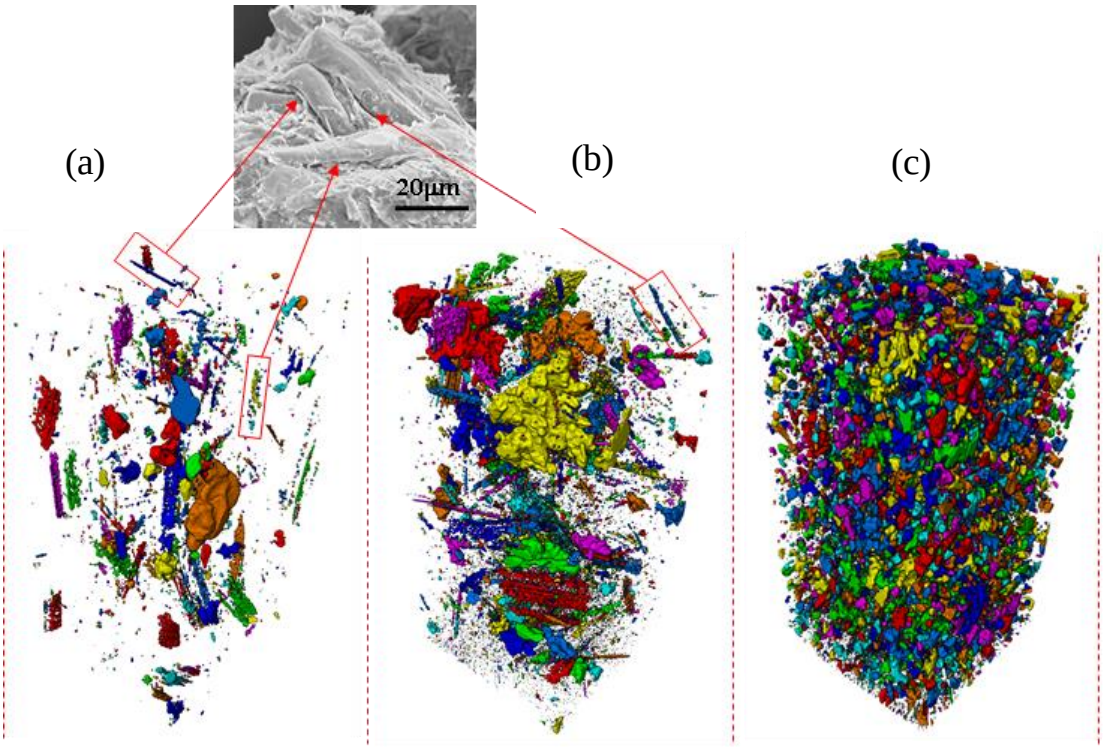

Figure 4 : The pore size distribution in biobased composites with PLA/PEG matrix reinforced with different fibers: (a) 30 wt% bamboo fibers, (b) 40 wt% bamboo fibers and (c) 50 wt% bamboo powders (Nguyen et al., 2022b).

3. Influence of pore characteristics on properties of materials

3.1. Mechanical properties

Porosity, pore size, pore size distribution, and the specific surface area are critical to the durability and mechanical properties of concrete (Zhang et al., 2017). Compressive strength is related to porosity and pore size and can be expressed as: $\sigma =$

$KC(1-P)/\sqrt{(r_{0.5})}$, where K is the constant of proportionality, C the cement content of concrete, P the porosity, and $r_{0.5}$ the mean pore radius distribution with the unit of nanometer (Das and Kondraivendhan, 2012). Not only compressive strength but also tensile strength both decrease with increased porosity and pore size, yet compressive strength is more dependent on porosity than tensile strength (Li et al., 2018). The increase in porosity may result in a decrease in the ratio of compressive strength to indirect tensile strength (Chen et al., 2013). Additionally, both compressive strength and freeze-thaw durability increase if the pore size is uniform and the distance between pores is large (Liu et al., 2020b). The concrete with a higher content of small pores (<0.01 mm^3) had a higher fatigue life, and a higher porosity may result in a lower fatigue life (Vicente et al., 2018). For basalt fiber reinforced concrete, the strength and fractural energy increased along the fractal dimension in the macropore region, while in the transition pore zone (diameter in the range of 20 nm to 50 nm), shrinkage strain linearly related to the fractal dimension (Li et al., 2020). The matrix strength of hybrid basalt-polypropylene fiber-reinforced concrete affected the cumulation pore volume, porosity, and volume fraction of pores at different scales (Niu et al., 2020).

3.2. Water permeability

Yu et al. (Yu et al., 2019) reported that the coefficient of permeability was linearly related to the ratio of total pore volume to total pore surface area. In 2D terms, the coefficient of permeability increased linearly with the pore area. In terms of 3D, the permeability coefficient increased along the pore volume, but its growth rate slowed down once the pore

volume was higher than 500 mm^3. The internal pore structure could lead to different permeability coefficients even with a similar porosity (Liu et al., 2020b). ANSYS FLUENT for Computational Fluid Dynamics analysis (CFD) could simulate concrete pressure (Wen et al., 2020). The maximum pressure was presented at the narrow pore near the entrance of the seepage flow and the pressure decreased more slowly with small aggregates with a small pore size (Figure 5). Zhang et al. (Zhang et al., 2018) used the triangular patches to compose connected pores in 3D, imported them into ICEM CFD software to repair the geometry, then imported them into another CFD software ANSYS FLUENT to simulate the water seepage flow, and finally the pressure contours of seepage flow (Figure 6) and the path lines (see detail in the reference) were obtained.

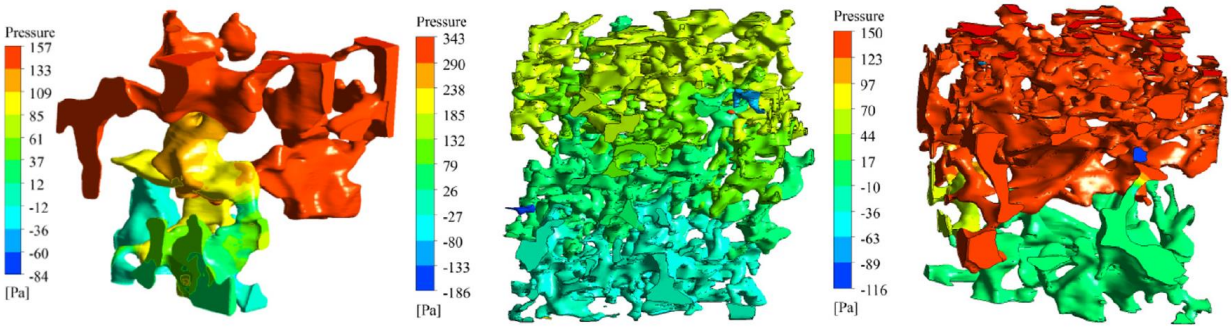

Figure 5 Pressure contours of seepage flow under pressure gradients of 3000 Pa/m in concretes composed of different sizes of aggregate: 5-10 mm (left), 10-15 mm (center), and 5-10 mm in the upper part and 10-15 mm in the lower part (right) (Wen et al., 2020).

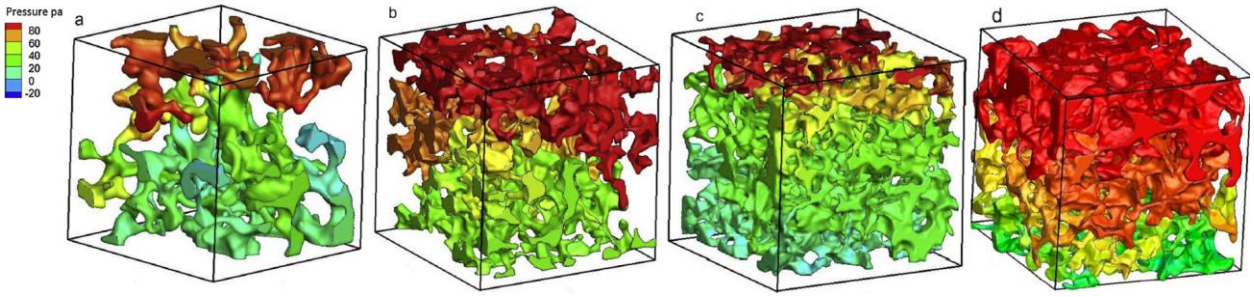

Figure 6 : Pressure contours of seepage flow under pressure inlet of 60 Pa in pervious concretes with different porosities (a) 13.2%, (b) 20.3%, (c) 24.8%, and (d) 28% (Zhang et al., 2018).

4. Image processing techniques application

4.1. Analyses of fiber distribution in porous materials

The image acquisition and processing method used in pores detection can also be used to detect the fiber distribution because the main knowledge is in common. In addition, the dynamic image analysis system (DIA) could be used to destructively detect the size and morphology of the particle or fiber (Bacaicoa et al., 2017), for instance, serials products of CAMSIZER could detect the particles in the range of 0.8 µm to 135 mm. Fibers are mainly presented as fold lines and curves in the concrete (Qin et al., 2019). Fiber distribution could be affected by many factors such as mixing time and fiber content. As shown in Figure 7, and the lowest and highest fiber densities were found in the top and bottom layers of the concrete, respectively, while a longer mixing time could improve the homogeneity of fiber distribution (Blaber et al., 2015). Fiber orientation depends on several factors, such as coarse aggregate (Qin et al., 2019), and printing process including fibers volume content, and nozzle size, but independent of print speed (Arunothayan et al., 2021). The orientation

of the fibers near the nozzle walls showed a higher possibility towards the printing direction than in the center of the nozzle, especially in the case of large nozzles (Arunothayan et al., 2021). Nguyen et al. (Nguyen et al., 2022b) reported about 50% of the bamboo fibers/powders reinforced in the PLA/PEG biobased composites. The distribution and orientation of bamboo fibers and powder were well observed in the composites, thanks to image processing by using aviso software, as shown in Figure 8. For the spraying fiber-reinforced concrete, the fibers were aligned perpendicular to the spray direction (Segura-Castillo et al., 2018). Concerning hemp lime concrete, it has an oriented internal structure that is determined by the direction of compacting force and the degree of orientation of hemp particles depends on the production method. Some image analysis methodologies have been also developed for the assessment of the frequency distributions of hemp shives orientation in hemp lime concrete of three compaction levels: 30, 45 and 60% volumetric decrease from the uncompact state. The results showed that the frequency distribution of particle orientations in the perpendicular plane is strongly swayed indicating the anisotropic material's structure. Based on a real-time observation technique, Marks et al. (Marks et al., 2021) reported that a different aspect ratio of formwork could lead to variations in concrete flow and end up with a different fiber orientation. In addition, the orientation of fibers varied during the casting time. 3D fiber distribution obtained by the different image acquisition and processing methods could be used to validate the models and distribution functions (Alberti et al., 2018).

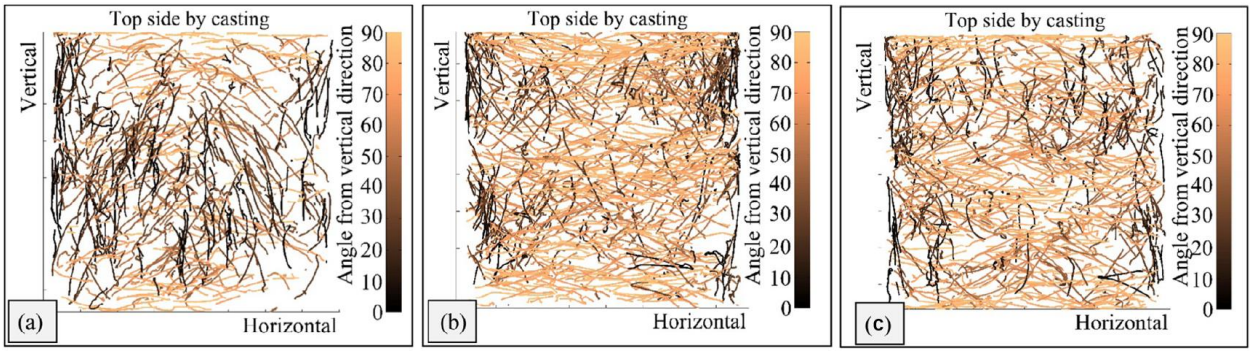

Figure 7 The projection of fibers on the x-y plane in the concrete. (a) 0.3%(v/v) fiber content after 5 mins of mixing (b) 0.5%(v/v) fiber content after 5 mins of mixing (c) 0.5%(v/v) fiber content after 30 mins of mixing (Blaber et al., 2015).

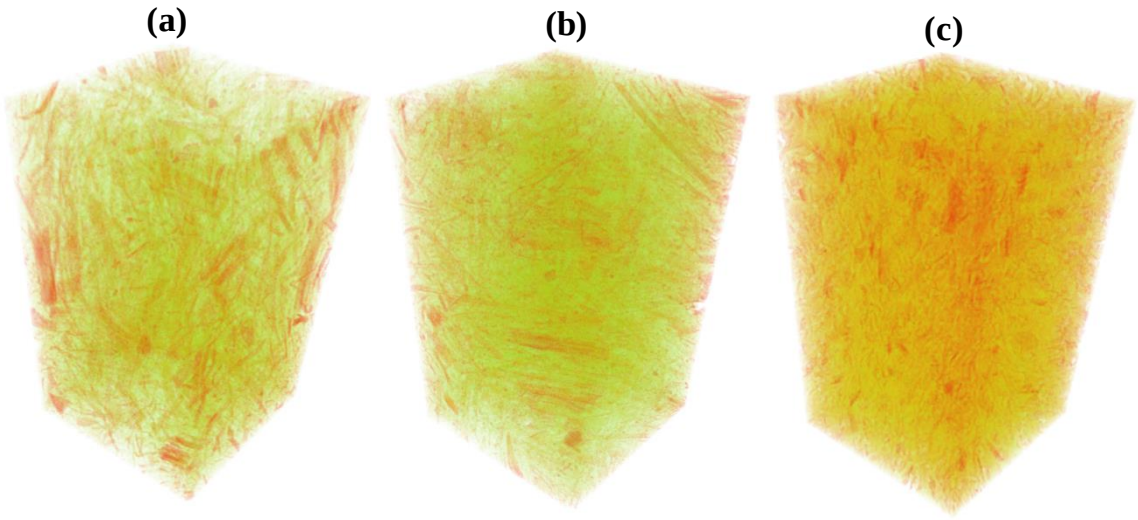

Figure 8 The distribution and orientation of bamboo fibers in PLA/GEG matrix composites: (a) 30 wt% fibers, (b) 40 wt% fibers and (c) 50 wt% powders. The resolution of scan was 5 μm, the images was analyzed by using Avizo software (Nguyen et al., 2022b) .

366 **4.2. The correlation between fiber distribution and the mechanical properties**

367 Normally, the addition of fibers could improve the mechanical properties of concrete. The
368 addition of fibers led to an improvement of the bending tensile strength by 11.23% and of
369 the compressive strength by 11.75% for concrete (Radojičić et al., 2022). The addition of
370 2% v/w bamboo fiber could improve the mechanical strength and static modulus of
371 elasticity of concrete (Ferreira et al., 2017). The flexural strengths of concrete could be
372 improved by 13.40% by the addition of aligned carbon fibers (Hambach et al., 2016). The
373 mechanical properties of concrete are also related to the properties of fibers, such as the
374 type of fibers in relation to the splitting tensile strengths (Hong et al., 2020), compressive
375 strength (Simões et al., 2017), and cracking resistance (Lyu et al., 2021), the length of
376 fibers in relation to the flexural strengths (Pham et al., 2020a; Schleiting et al., 2020) and
377 tensile strain (Ahmed and Maalej, 2009), aspect-ratio of fibers in relation to the flexural
378 strength (Schleiting et al., 2020), the volume content of fibers in relation to the flexural
379 strengths, but not to the compressive strength (Kang et al., 2021). Besides, the compressive
380 and flexural strength of concrete can also be affected by fiber distribution, which is more
381 related to the manufacturing methods of concrete. Raju et al. (Raju et al., 2020) also
382 indicated that better fiber distribution and orientation could increase fiber content in the
383 direction of improved flexural strength. The manufacture modes, which affected the fiber
384 distribution, might affect the compressive strengths of concrete as well. The printed high-
385 performance fiber-reinforced concrete was reported had a higher compression strength than
386 the cast concrete, while no significant difference was found in the case of ultra-high-

performance steel reinforced concrete (Arunothayan et al., 2021). The printed concrete reinforced with polyvinyl alcohol or polypropylene based fiber had a complex compressive and flexural strength, and both compressive and flexural strength differed in the x and z directions compared to casted specimens (Pham et al., 2021). In addition, for the sprayed fiber-reinforced concrete, the load parallel to the spray direction was measured to be 3.5 times greater than the perpendicular load (Segura-Castillo et al., 2018).

It should be noted that machine learning can also be used in the field of fiber-reinforced concrete. Manca et al. (Manca et al., 2018) used the machine learning algorithm to detect fiber modes based on 2D images acquired by a normal digital camera. For the training, 4350 “snap” and “pull-out” fiber images were first labeled and then the Linear Support Vector Machine model was applied to recognize those two categories with an accuracy of 91%. Finally, the position, failure modes, length, orientation, and amount of fibers were detectable. Based on the above steps, Manca et al. (Manca et al., 2018) detected that the macro synthetic fiber would snap if the fiber orientation was in the same direction as the main stress. A model based on the Finite Element Method, including the input of the spatial and angular orientation of fibers and the pore size distribution, was used to simulate the elastic properties of polypropylene fiber-reinforced concrete and the numerical result was consistent with the experiment result (Trofimov et al., 2018).

4.3. DIC applied to the evaluation of surface deformation and cracks

Digital Image Correlation (DIC) is a non-destructive method that is normally used to measure the displacement and strains in full field. DIC can be used for both real-time

(Rucka et al., 2021) and delayed-time observation and it progressed and is applied in a wide field. Articles searched on Web of Science with the keyword “Digital Image Correlation” have increased from 1 in 1975 to 427 in 2010 and continue to increase to 1482 in 2020. DIC can be subdivided into 2D-DIC (based on two-dimensional images, Figure 9a), StereoDIC (or 3D-DIC, based on three-dimensional images from multiple camera orientations, Figure 9b), and Digital Volume Correlation (DVC or VDIC, based on three-dimensional tomographic images from CT or other machines, Figure 9c), therefore, some pros and cons are common (Bouterf et al., 2020; Sutton and Hild, 2015). The detailed history and technique of DIC can be found in (Pan, 2018). The observation of advanced 4D images, which consist of 3D space and time, has also developed, and attracted attention. In addition, the characterization of concrete behavior under cyclic loading was studied using 2D digital image correlation (Bello et al., 2023). The rapid development of photographic technology, especially 3D techniques, such as X-ray imaging, Magnetic Resonance Imaging (MRI), atomic force microscope (AFP), and scanning tunnel microscope (STM) (Pan, 2018) and corresponding image processing and analysis method are being developed and widely used in the field of mechanical analysis. Some commercial software helps users perform DIC analysis, such as SeptD, VIC-2/3D, StrainMaster, GOM-2/3D, and Image processing toolbox in MATLAB. In addition, some open-source software such as Python-based TomoWarp2 (Tudisco et al., 2017), and MATLAB-based Ncorr (Blaber et al., 2015) are widely used as well. In the field of concrete, searching “Digital Image Correlation” and “Concrete” on the Web of Science, there are 1073 papers up to

29/02/2021, and 202 papers in 2020.

For example, Nguyen et al. (Nguyen et al., 2018b) obtained a series of images using the LaVision StrainMaster optical system and recorded the load over time by Zwick device, the DIC software of StrainMaster and VIC-2D was used to measure the full-field displacement and calculated the tensile and fracture distribution. Based on the full-field displacement obtained via DIC technology, Liu et al. (Liu et al., 2020a) divided the flexural damage process into a microcrack initiation phase, a macrocrack evolution phase, and a main crack propagation phase. DIC was also used to study the failure of the concrete with different types of fiber (Melenka and Carey, 2015), detect the crack propagation in real-time (Figure 10a-d) (Rucka et al., 2021), monitor the shear and principle strain of the fiber-reinforced concrete (Figure 10e) (Flansbjer et al., 2018; Lakavath et al., 2019; Picazo et al., 2018). A series of works and examples of DVC was presented in an update of reviews (Bouterf et al., 2020; Buljac et al., 2018; Sutton and Hild, 2015). However, it remains difficult to process such a large dataset in real time and keep the specimen static during the load test.

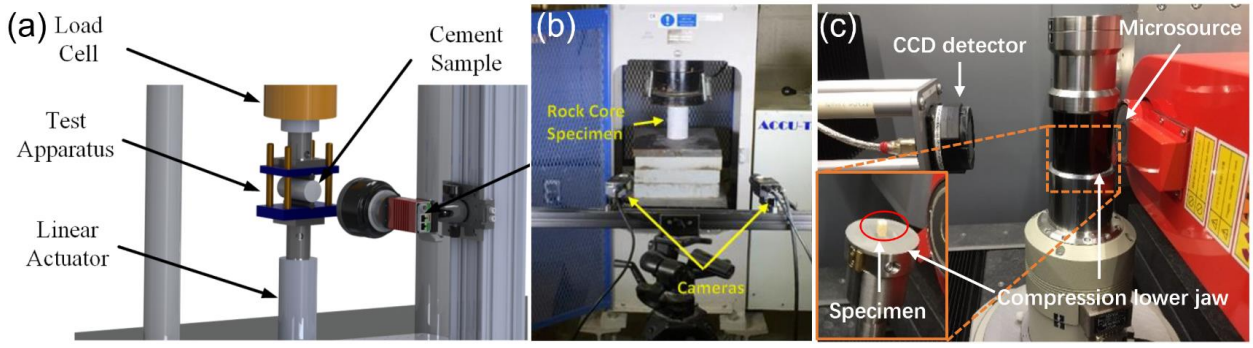

Figure 9: 9 Setup of 2D-DIC (a) (Melenka and Carey, 2015), 3D-DIC (b) (Abdulqader and Rizos, 2020), and DVC (c) (Nguyen et al., 2021a).

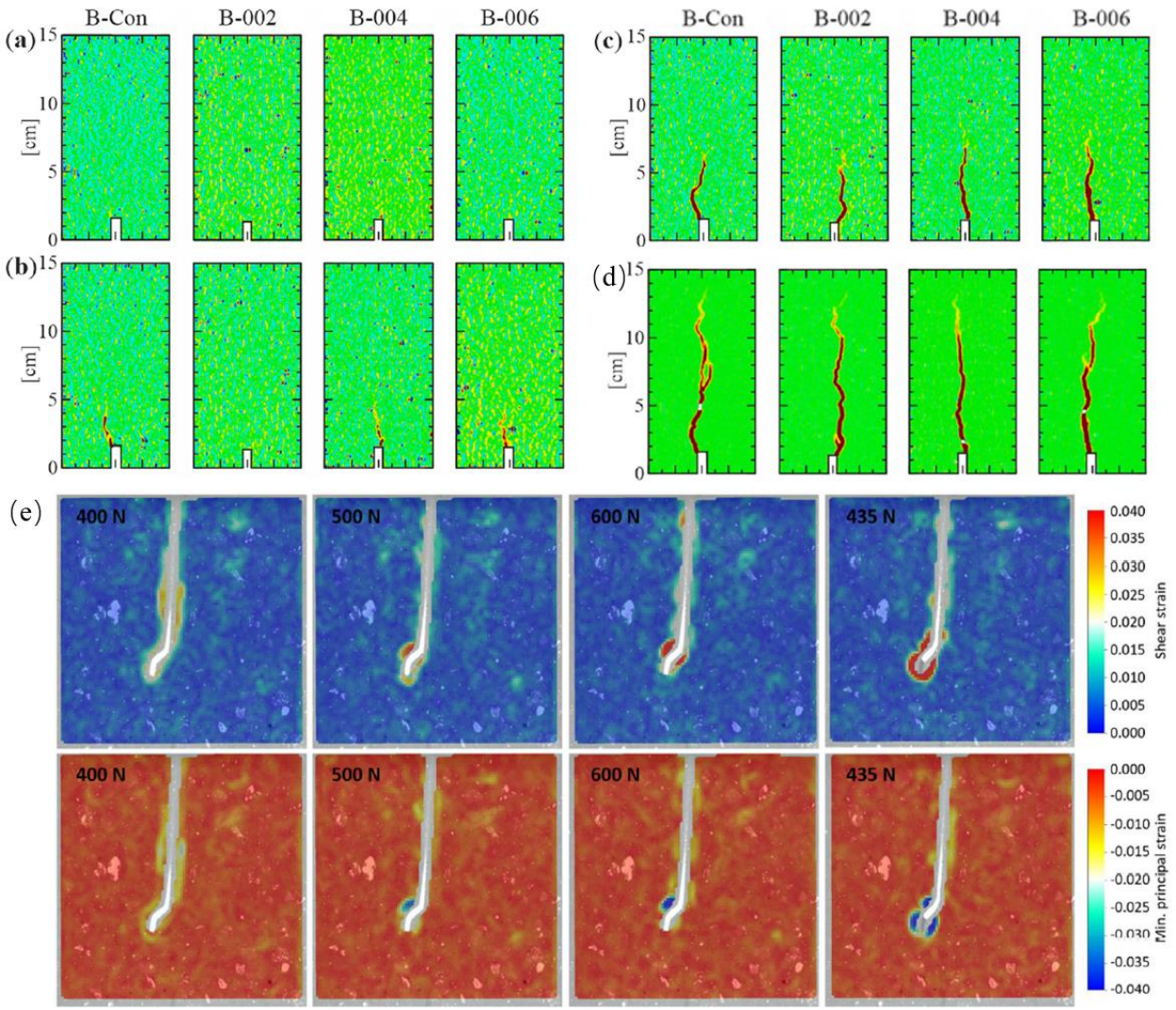

Figure 10: (a-d) 2D-DIC analysis. Cracking evolution of concrete with different content fibers at different time instances: (a) the load value equals to 90% of the maximum force (F_{max}) before reaching the peak value, (b) F_{max}, (c) 90% post-F_{max}, and (d) crack mouth opening displacement equals 0.3 mm. B-con, B-002, B-004, B-006 represent the macro polymer fiber content of 0, 2 kg/m^3, 4 kg/m^3 and 6 kg/m^3, respectively (Rucka et al., 2021). (e) DVC analysis: shear and principle strain of the hooked fiber concrete (Flansbjer et al., 2018).

4.4. Tortuosity calculation

The tortuosity is defined as the ratio of the preferential length of fluid pathways to the straight-line distance in the microstructure. Tortuosity is an important parameter that significantly affects the transport behavior of fluid, molecular diffusion, heat transfer within porous materials. Therefore, the mass and heat transfer inside the porous material depends greatly on its tortuosity value. Accurate determination of this value allows accurate assessment and prediction of multi-physics properties including acoustic properties, effective diffusivity, thermal insulation, and permeability of porous materials. To date, there are several approaches to determining the tortuosity of porous materials such as experimental, numerical, and analytical methods (Laudone et al., 2015; Morin et al., 2010; Wu et al., 2018). These methods have been applied to directly measure tortuosity value or some models have been also developed to compute the tortuosity in two-dimensional (2D) and even three-dimensional (3D) configurations. Therefore, a 3D pore network modeling was used to calculate the tortuosity of porous media by using network elements for connecting each pore to neighbors in a random direction. The tortuosity of sandstone was computed by this model, and it showed a good agreement with the experimental data (Nemati et al., 2020). However, these methods still have many limitations in determining the tortuosity value of porous structures with irregular voids sizes of the realistic porous materials. Furthermore, they could not fully describe the relationship between the porous structure (void space distribution and pore connectivity) and tortuosity (Zhao and Zhou, 2022).

The emergence of X-ray CT imaging techniques today combined with image processing techniques has opened an interesting approach to porous structures materials. The application of this technique was not small in adding useful approaches to the previously developed techniques related to the calculation of microstructure parameters from 3D images such as porosity, pore distribution, and pore sizes (Nguyen et al., 2021a; Nguyen et al., 2022a). Specifically, this technique was also gradually being applied in exploring the tortuosity of porous materials to explain its influence on microscopic permeability and heat and mass transfer in different fields. Accordingly, the 3D pore models reconstructed from 2D projections from tomography allowed to calculate pore size distribution and permeability of sandstone (Zhao and Zhou, 2019). The tortuosity and pore connectivity of porous alumina structures were identified according to its 3D images obtained from X-ray CT (Shanti et al., 2014). The X-ray μCT imaging techniques allowed extraction of the porosity and tortuosity of different types of sandstone using a labeling segmentation algorithm. It allowed to present the relation between tortuosity and pore characteristics (pore size and pore shape). The finding helps to evaluate the pore-scale permeability and diffusivity of geomaterials in the field of geothermal exploration (Zhao and Zhou, 2022).

4.5. Liquid imbibition/drying mechanism in porous materials

The advent of imaging technology and image processing tools has significantly supported the morphological studies of the internal structure of materials, especially, multi-component and porous structures materials. The interactions between water and wood and wood-derived materials have also been specifically observed through 2D and 3D imaging

observations. Accordingly, water imbibition to wood in different directions was studied by 3D imaging technique using 2D image series obtained from high-resolution X-ray tomography (Perré et al., 2022). Accordingly, the cylindrical wood sample is prepared with a diameter of several centimeters. The sample was then continuously exposed to a water source and placed inside the chamber of the tomography device. The penetration of water into the sample was studied through continuous in-situ scanning on this device at different time intervals. A series of 2D images obtained from this scan are processed through various image processing techniques to analyze the process and movement of liquid water within the porous structure of the wood. Accordingly, in the literature, the liquid water imbibition to Norway spruce wood (softwood) was studied using X-ray tomography in longitudinal direction (Martin et al., 2022). The sample preparation and experimental design were described in Figure 11. A series of 2D projections were obtained from the scanning of the device which were then processed with MATLAB to observe the mechanism of water permeation along the pathways inside the microstructure of the wood in different directions (radial tangential and longitudinal). The result has contributed to explain the mechanism of liquid water transmission inside earlywood and latewood of Norway spruce wood (softwood). Accordingly, the study concluded that several different fluid transfer mechanisms were observed inside Norway spruce wood for earlywood and latewood regions, respectively. However, this study did not consider the movement of the measuring point linked to the swelling and shrinkage of the wood samples.

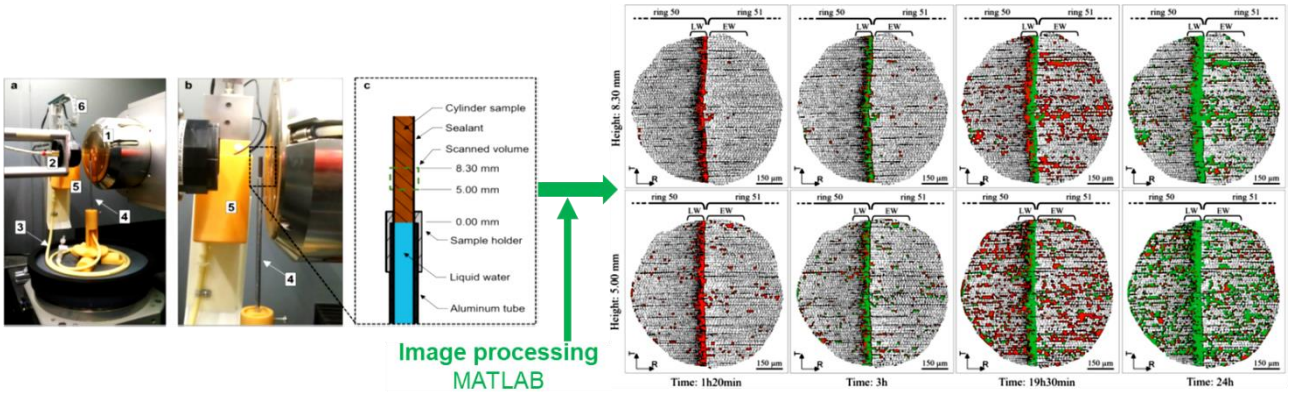

517

518 Figure 11: Water imbibition in Norway spruce wood: (a) experimental setup in the
519 tomography with nano X-ray source; (b) wood specimen placed between the nano X-ray
520 source and CCD camera; (c) schema of the experimental setup and 3D scans volume and
521 position; and (d) cross-section of the wood surface during imbibition at different time
522 (Martin et al., 2022).

523 The mechanism of fluid transfer (water and oil) in hardwood and softwood was also
524 performed using X-ray tomography combined with Avizo image analysis technique (Perré
525 et al., 2022). The observed results added significantly to the comparison and explanation
526 of the fluid transport mechanism of different liquids (polar and non-polar) within the
527 complex porous structure of two different woods (poplar and spruce). Accordingly, spruce
528 and poplar were prepared in cylinders with a diameter of about 3-4 cm. The samples were
529 then exposed to the liquid and scanned at different times using a tomography device with
530 micro-source and CCD camera at 3.6 µm resolution. The samples were reconstructed in
531 3D through 2D projections through AVIZO image processing software. The images were
532 processed using ImageJ. The results showed that there is a great difference in the

mechanism of water and oil penetration into the wood. Accordingly, the oil penetrates the wood at a very fast rate and spreads through the gaps inside the wood under the action of capillary force. Meanwhile, water penetrates the wood very slowly and penetrates the cell walls of the wood before being present in the voids inside the wood, as presented in Figure 12.

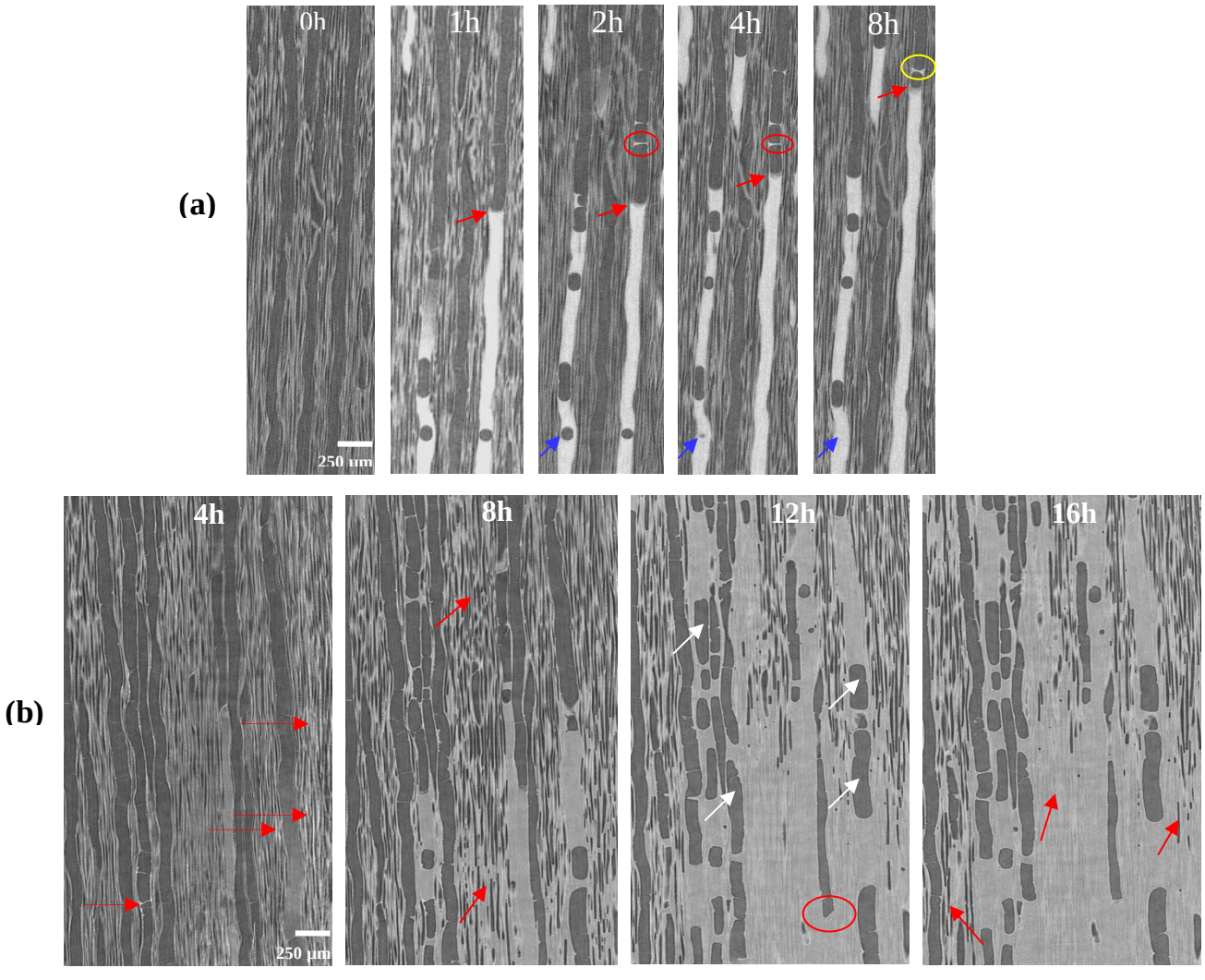

Figure 12: The 3D slide observation of liquid imbibition in poplar using tomography at a resolution of 3.6 µm, the images were processed using ImageJ: (a) oil imbibition

554 and (b) water imbibition (Perré et al., 2022).

555 Thus, studying the mechanism of liquid imbibition into the wood through imaging
556 techniques (2D or 3D) has contributed significantly to understanding the mechanism and
557 behavior of liquid transport into the internal microstructure of different wood. The time, it
558 takes to reach saturation and the structural change of the wood under the impact of water,
559 provides early warning of potential consequences occurring in actual buildings. However,
560 the limitation of the imaging technique does not allow to quantify the amount of water
561 absorbed into the wood accurately because the contrast of the water and the fibers of the
562 wood could not be clearly distinguished during the image processing. In addition, it is
563 necessary to consider in the analysis the coupling between the diffusion of the liquid and
564 the deformation of the pores. Furthermore, the limitation of the technique is not being able
565 to detect signs of water inside the wood makes it impossible to accurately quantify the
566 water content. Moreover, current experimental designs face many difficulties in integrating
567 measurement methods in image acquisition experiments such as in-situ experiments on
568 tomography equipment or synchrotrons.

569 The combination of image analysis techniques with the quantification method allowed to
570 measure the mass change of wood in the presence of oil and water, which allows the
571 calculation of the liquid penetration time to reach the saturation level inside the wood, as
572 shown in Figure 13. The results showed that the oil penetration was actually very fast and
573 quickly ended with its presence on the top of the sample. At this point, the penetration of

oil seemed to slow down and ended through the saturation curve (plateau) and the amount of oil entering the wood was very small because the oil only penetrated the interconnected spaces inside the sample, not the cell wall. Meanwhile, the kinetics of water imbibition into wood was very slow because water penetrated the cell wall of the wood before being present in the voids of the wood. Therefore, it took a very long time to achieve saturation and the amount of water entering the wood was also considerable.

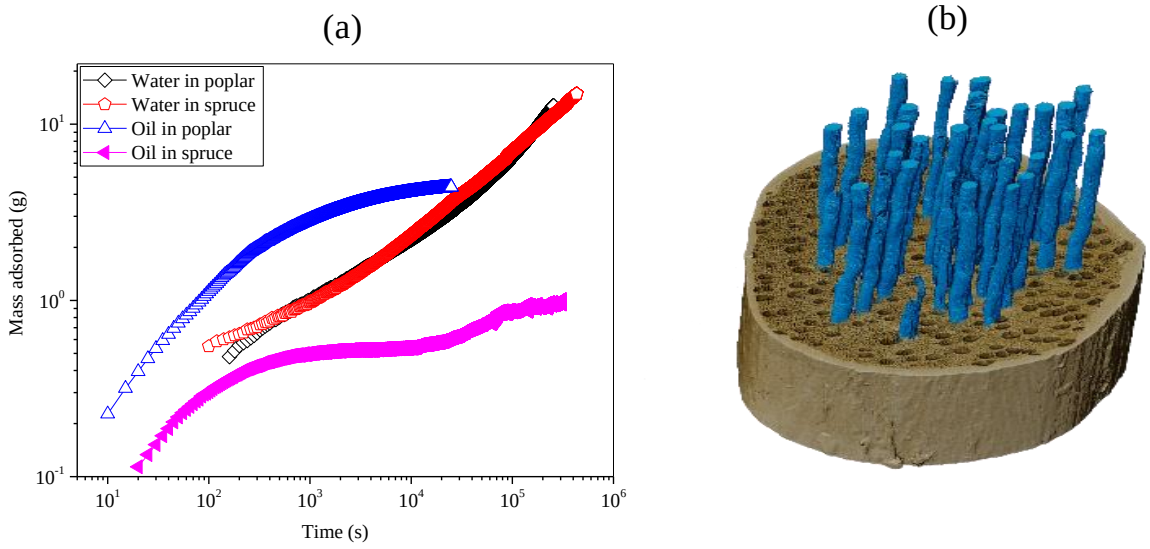

Figure 13: The dynamics of water and silicone oil imbibition in poplar and spruce: (a) evolutions of mass absorbed of the liquid into the wood with time and (b) a miniature scale in 3D volume observation of the internal structure of poplar after 2 h of silicone oil imbibition test (Perré et al., 2022).

Furthermore, the amount of water and oil absorbed inside the poplar by experimental time was also quantified by NMR method (Nguyen et al., 2020). Compared to X-ray tomography, this method also allowed quantification of the free water content present in

595 the sample based on its T_2 relaxation. The water bounding to the cell wall of the wood was
596 calculated based on the swelling coefficient of the wood (Zhou et al., 2018). Thus, the
597 combination of quantitative methods and imaging techniques allows a profound
598 understanding of the nature and mechanism of water absorption into the wood. It also
599 allowed to explain the difference in the mechanism of water penetration of different wood
600 species (Nguyen et al., 2020; Zhou et al., 2018). Up to now, this is the technique that can
601 most accurately quantify the volume of liquid penetrating and moving inside porous
602 materials. This technique also allows the observation of 2D images at different positions
603 of the sample as well as different directions of the porous materials.
604 Finally, one of the interesting applications of current imaging techniques is to allow the
605 observation of fluid transmission in porous materials in 4D (3D observations with time).
606 Accordingly, the penetration and migration of the oil and water in spruce and poplar have
607 been studied in 4D observation, as shown in Figure 14 (Perré et al., 2022).

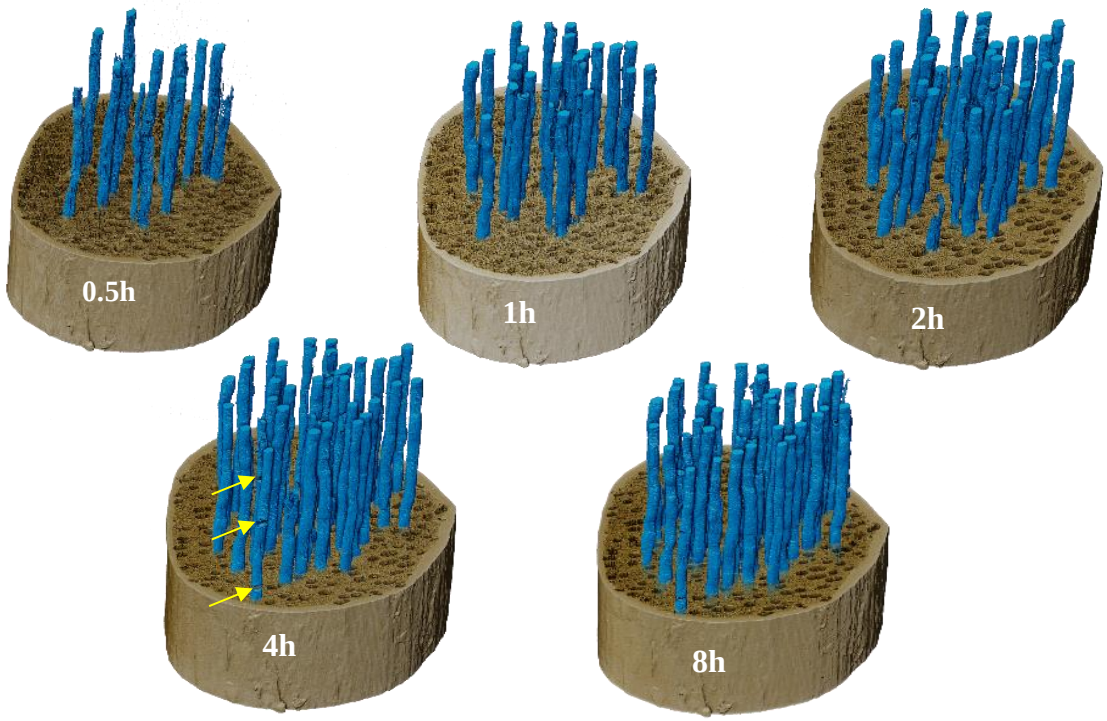

608

609 Figure 14: The 3D volumetric observation of the dynamics of silicone oil imbibition in

610 poplar samples at different times (4D) (Perré et al., 2022).

611 According to these 4D observations, the oil moves at a very rapid rate from the beginning

612 inside the pores and voids of the wood and rapidly reaches saturation afterward whereas,

613 at the same time, the penetration and migration of water is very slow. Furthermore,

614 different transmission mechanisms of liquids of different natures in porous materials were

615 also discovered in this study. Another interesting physical transport phenomenon also

616 detected in 4D observation was the existence and migration of air bubbles inside the pores.

617 They tend to decrease in volume and then appear to be compressed to the smallest volume

618 (see yellow arrows in Figure 14). Until now, several imaging techniques and image

processing software used to study the transfer of liquids (water and oil) inside porous materials such as wood and bio-based materials were summarized in Table 1 which helps the user to choose the most suitable one.

Table 1: Some imaging techniques used to analyze liquid migration in porous materials

Materials	Image technique	Dimension	Image processing methods	References
Poplar and spruce	Tomography	3D	Avizo, ImageJ	(Perre et al., 2022)
Norway spruce wood	Tomography	3D	Matlab	(Martin et al., 2022)
Norway spruce	Tomography	2D	Matlab	(Martin et al., 2022)
Douglas-fir	MRI	2D	ImageJ	(Nguyen et al., 2021b)
Poplar	MRI	2D	Image J	(Zhou et al., 2018)
Hemp concrete	MRI	2D	-	(Fu et al., 2021)
Coal	Tomography	3D	Avizo	(Lu et al., 2022)

Hornbeam	Synchrotron	3D	-	(Zhou et al., 2019)
Hornbeam	MRI	2D	-	(Zhou et al., 2019)

Finally, based on observations and data obtained from experiments, the 1D and 2D modeling were developed to simulate oil and water imbibition in the vessels and fibers of the poplar and spruce. Four simulations were applied, with assumptions inferred from the 3D microstructural observations (Perré et al., 2022). Accordingly, the 3D experimental observations were used to develop a simple imbibition model that satisfactorily simulates macroscopic imbibition kinetics. The 1D modeling approach is dedicated to oil imbibition in poplar and spruce while a 2D modeling approach is developed for water imbibition in poplar and spruce.

5. Conclusions

This paper has provided knowledge related to the image techniques used today to study the microstructure of porous materials including wood and bio-based materials from natural fibers by 3D approach. A variety of imaging techniques and image processing methods were analyzed, focusing on the microstructure including porosity, distribution and size of pores and fibers in the porous materials. In addition, these techniques were also used to explain the mechanism of penetration and movement of liquids (oil and water) into porous materials, which are intended to confirm the hypotheses and explain the results obtained

by the simulation as well as the experimental methods in the previous works. This paper also provides 4D observation of fluid movement inside porous materials, thereby allowing to explain the mechanisms of transport of polar and non-polar fluids inside bio-based materials. However, the main drawback of the image processing technique is the quantification of components within bio-based materials as well as the mass or volume of water changes in porous materials. This was due to the similar or close densities or signals of the components, which made it impossible to accurately distinguish each specific component, thereby causing incorrect quantification. Therefore, further studies should develop advanced techniques, possibly supported by artificial intelligence (IA), to enable more efficient quantification of this image processing technique. Furthermore, the resolutions of the analytical methods should be increased to obtain high image quality and to identify the smallest possible pore size to study more accurately of the porous properties of materials. Finally, the image analytical methods should be integrated with loading, temperature and humidity controllers to study their influence on the comprehensive properties of porous materials.

Acknowledgements

This study was done within the ANR-21-CE22-0026 project. The authors wish to thank the French National Research Agency (ANR) for financial support.

References

Abdulqader, A., Rizos, D. C., 2020. Advantages of using digital image correlation techniques in uniaxial compression tests. Results in Engineering 6, 100109.

661 Ahmed, S. F. U., Maalej, M., 2009. Tensile strain hardening behaviour of hybrid steel-
662 polyethylene fibre reinforced cementitious composites. Construction and Building
663 Materials 23, 96-106.
664 Alberti, M. G., Enfedaque, A., Gálvez, J. C., 2018. A review on the assessment and
665 prediction of the orientation and distribution of fibres for concrete. Composites Part B:
666 Engineering 151, 274-290.
667 Arashpour, M., Ngo, T., Li, H., 2021. Scene understanding in construction and buildings
668 using image processing methods: A comprehensive review and a case study. Journal of
669 Building Engineering 33, 101672.
670 Arunothayan, A. R., Nematollahi, B., Ranade, R., Bong, S. H., Sanjayan, J. G., Khayat, K.
671 H., 2021. Fiber orientation effects on ultra-high performance concrete formed by 3D
672 printing. Cement and Concrete Research 143, 106384.
673 Bacaicoa, I., Lütje, M., Sälzer, P., Umbach, C., Brückner-Foit, A., Heim, H.-P.,
674 Middendorf, B., 2017. Comparative investigation of two-dimensional imaging methods
675 and X-ray tomography in the characterization of microstructure 59, 829-836.
676 Bello, I., González-Fontebo, B., Wardeh, G., Martínez-Abella, F., 2023. Journal of
677 Building Engineering. Characterization of concrete behavior under cyclic loading using 2D
678 digital image correlation 78, 107709.
679 Blaber, J., Adair, B., Antoniou, A., 2015. Ncorr: Open-Source 2D Digital Image
680 Correlation Matlab Software. Experimental Mechanics 55, 1105-1122.
681 Bordelon, A. C., Hong, S., Bearzi, Y., Vachet, C., Gerig, G., 2020. Visualizing Air Voids
682 and Synthetic Fibers from X-Ray Computed Tomographic Images of Concrete. 2020
683 Intermountain Engineering, Technology and Computing (IETC), pp. 1-6.
684 Borges de Oliveira, F., Stolfi, A., Bartscher, M., De Chiffre, L., Neuschaefer-Rube, U.,
685 2016. Experimental investigation of surface determination process on multi-material
686 components for dimensional computed tomography. Case Studies in Nondestructive
687 Testing and Evaluation 6, 93-103.
688 Bouterf, A., Buljac, A., Hild, F., Jailin, C., Neggers, J., Roux, S., 2020. Digital Volume
689 Correlation of Laminographic and Tomographic Images: Results and Challenges. pp. 3-20.
690 Buljac, A., Jailin, C., Mendoza, A., Neggers, J., Taillandier-Thomas, T., Bouterf, A.,
691 Smaniotto, B., Hild, F., Roux, S., 2018. Digital Volume Correlation: Review of Progress
692 and Challenges. Experimental Mechanics 58, 661-708.
693 Carlson, J., Sutter, L., Van Dam, T., Peterson, K., 2006. Comparison of Flatbed Scanner
694 and RapidAir 457 System for Determining Air Void System Parameters of Hardened
695 Concrete. Transportation Research Record 1979, 54-59.
696 Chen, X., Wu, S., Zhou, J., 2013. Influence of porosity on compressive and tensile strength
697 of cement mortar. Construction and Building Materials 40, 869-874.
698 Chung, S.-Y., Sikora, P., Rucinska, T., Stephan, D., Abd Elrahman, M., 2020. Comparison
699 of the pore size distributions of concretes with different air-entraining admixture dosages
700 using 2D and 3D imaging approaches. Materials Characterization 162, 110182.

Das, B. B., Kondraivendhan, B., 2012. Implication of pore size distribution parameters on compressive strength, permeability and hydraulic diffusivity of concrete. Construction and Building Materials 28, 382-386.
du Plessis, A., Boshoff, W. P., 2019. A review of X-ray computed tomography of concrete and asphalt construction materials. Construction and Building Materials 199, 637-651.
Engelund, E. T., Thygesen, L. G., Svensson, S., Hill, C. A. S., 2013. A critical discussion of the physics of wood–water interactions. Wood Science and Technology 47, 141-161.
Ferreira, C., Tavares, S., Ferreira, B., Fernandes, A., Fonseca, S., Oliveira, C., Teixeira, R., Gouveia, L., 2017. Comparative Study About Mechanical Properties of Strutural Standard Concrete and Concrete with Addition of Vegetable Fibers. Materials Research 20, 102-107.
Flansbjer, M., Portal, N. W., Hall, S., Engqvist, J., 2018. Analysis of Failure Modes in Fiber Reinforced Concrete Using X-ray Tomography and Digital Volume Correlation. Proceedings.
Fu, J., Thomas, H. R., Li, C., 2021. Tortuosity of porous media: Image analysis and physical simulation. Earth-Science Reviews 212, 103439.
Hambach, M., Möller, H., Neumann, T., Volkmer, D., 2016. Portland cement paste with aligned carbon fibers exhibiting exceptionally high flexural strength (> 100MPa). Cement and Concrete Research 89, 80-86.
Hong, L., Chen, Y. D., Li, T. D., Gao, P., Sun, L. Z., 2020. Microstructure and bonding behavior of fiber-mortar interface in fiber-reinforced concrete. Construction and Building Materials 232, 117235.
Kang, M.-C., Yoo, D.-Y., Gupta, R., 2021. Machine learning-based prediction for compressive and flexural strengths of steel fiber-reinforced concrete. Construction and Building Materials 266, 121117.
Lai, J., Wang, G., Wang, Z., Chen, J., Pang, X., Wang, S., Zhou, Z., He, Z., Qin, Z., Fan, X., 2018. A review on pore structure characterization in tight sandstones. Earth-Science Reviews 177, 436-457.
Lakavath, C., Joshi, S. S., Prakash, S. S., 2019. Investigation of the effect of steel fibers on the shear crack-opening and crack-slip behavior of prestressed concrete beams using digital image correlation. Engineering Structures 193, 28-42.
Laudone, G. M., Gribble, C. M., Jones, K. L., Collier, H. J., Matthews, G. P., 2015. Validated a priori calculation of tortuosity in porous materials including sandstone and limestone. Chemical Engineering Science 131, 109-117.
Li, D., Li, Z., Lv, C., Zhang, G., Yin, Y., 2018. A predictive model of the effective tensile and compressive strengths of concrete considering porosity and pore size. Construction and Building Materials 170, 520-526.
Li, Y., Shen, A., Wu, H., 2020. Fractal Dimension of Basalt Fiber Reinforced Concrete (BFRC) and Its Correlations to Pore Structure, Strength and Shrinkage 13, 3238.
Lim, S., Lee, H.-S., Kawashima, S., 2018. Pore structure refinement of cement paste incorporating nanosilica: Study with dual beam scanning electron microscopy/focused ion beam (SEM/FIB). Materials Characterization 145, 323-328.

743 Liu, B., Guo, J., Wen, X., Zhou, J., Deng, Z., 2020a. Study on flexural behavior of carbon
744 fibers reinforced coral concrete using digital image correlation. Construction and Building
745 Materials 242, 117968.
746 Liu, R., Chi, Y., Chen, S., Jiang, Q., Meng, X., Wu, K., Li, S., 2020b. Influence of Pore
747 Structure Characteristics on the Mechanical and Durability Behavior of Pervious Concrete
748 Material Based on Image Analysis. International Journal of Concrete Structures and
749 Materials 14, 29.
750 Lu, Y., Liu, D., Cai, Y., Li, Q., Zhou, Y., 2022. Spontaneous imbibition in coal with in-
751 situ dynamic micro-CT imaging. Journal of Petroleum Science and Engineering 208,
752 109296.
753 Luo, S., Lutkenhaus, J. L., Nasrabadi, H., 2019. Experimental study of pore size
754 distribution effect on phase transitions of hydrocarbons in nanoporous media. Fluid Phase
755 Equilibria 487, 8-15.
756 Lyu, Z., Shen, A., Meng, W., 2021. Properties, mechanism, and optimization of
757 superabsorbent polymers and basalt fibers modified cementitious composite. Construction
758 and Building Materials 276, 122212.
759 Ma, K., Huang, X., Shen, J., Hu, M., Long, G., Xie, Y., Zeng, X., Xu, Z., Zhang, W., 2021.
760 The morphological characteristics of brick-concrete recycled coarse aggregate based on
761 the digital image processing technique. Journal of Building Engineering, 103292.
762 Manca, M., Karrech, A., Dight, P., Ciancio, D., 2018. Image Processing and Machine
763 Learning to investigate fibre distribution on fibre-reinforced shotcrete Round Determinate
764 Panels. Construction and Building Materials 190, 870-880.
765 Marks, B., Miletić, M., Lee, B. C. H., Zia, M. H., Barros, J. A. O., Dias-da-Costa, D., 2021.
766 Monitoring steel fibre orientation in self-compacting cementitious composite slabs during
767 pouring with dynamic X-ray radiography. Cement and Concrete Research 143, 106390.
768 Martin, B., Colin, J., Perré, P., Casalinho, J., Mounkaila, M., Lu, P., Rémond, R., 2022. CT
769 investigation of 3D liquid pathways in the anatomical structure of Norway spruce wood
770 during imbibition 76, 592-603.
771 Melenka, G., Carey, J., 2015. Evaluation of Fiber Reinforced Cement Using Digital Image
772 Correlation. PLoS ONE 10, e0128644.
773 Moravcová, B., Põssl, P., Misák, P., Blažek, M., 2016. Possibilities of determining the air-
774 pore content in cement composites using computed tomography and other methods.
775 Materiali in tehnologije 50, 491-498.
776 Morin, R. H., LeBlanc, D. R., Troutman, B. M., 2010. The Influence of Topology on
777 Hydraulic Conductivity in a Sand-and-Gravel Aquifer 48, 181-190.
778 Nemati, R., Rahbar Shahrouzi, J., Alizadeh, R., 2020. A stochastic approach for predicting
779 tortuosity in porous media via pore network modeling. Computers and Geotechnics 120,
780 103406.
781 Nguyen, D. M., Almeida, G., Nguyen, T. M. L., Zhang, J., Lu, P., Colin, J., Perré, P.,
782 2021a. A Critical Review of Current Imaging Techniques to Investigate Water Transfers
783 in Wood and Biosourced Materials. Transport in Porous Media 137, 21-61.

784 Nguyen, D. M., Care, S., Courtier-Murias, D., Zhou, M., Coussot, P., 2021b. Mechanisms
785 of liquid imbibition in Douglas-fir inferred from 1H nuclear magnetic resonance methods
786 75, 225-236.
787 Nguyen, D. M., Caré, S., Courtier-Murias, D., Zhou, M., Coussot, P., 2020. Mechanisms
788 of liquid imbibition in Douglas-fir inferred from 1H Nuclear Magnetic Resonance
789 methods. Holzforschung.
790 Nguyen, D. M., Diep, T. M. H., da Silva, Y. F., Vu, T. N., Hoang, D., Thuc, C. N. H., Bui,
791 Q. B., Perré, P., 2022a. Three-dimensional pore characterization of
792 poly(lactic)acid/bamboo biodegradable panels. International Journal of Biological
793 Macromolecules 221, 16-24.
794 Nguyen, D. M., Diep, T. M. H., Silva, Y. F., Vu, T. N., Hoang, D., Q,, Ha-Thuc, C. N.,
795 Bui, Q. B., Perré, P., 2022b. Three-dimensional pore characterization of
796 poly(lactic)acid/bamboo biodegradable panels. International Journal of Biological
797 Macromolecules 30, 16-24.
798 Nguyen, D. M., Grillet, A.-C., Bui, Q.-B., Diep, T. M. H., Woloszyn, M., 2018a. Building
799 bio-insulation materials based on bamboo powder and bio-binders. Construction and
800 Building Materials 186, 686-698.
801 Nguyen, D. M., Grillet, A.-C., Diep, T. M. H., Ha Thuc, C. N., Woloszyn, M., 2017.
802 Hygrothermal properties of bio-insulation building materials based on bamboo fibers and
803 bio-glues. Construction and Building Materials 155, 852-866.
804 Nguyen, H., Carvelli, V., Adesanya, E., Kinnunen, P., Illikainen, M., 2018b. High
805 performance cementitious composite from alkali-activated ladle slag reinforced with
806 polypropylene fibers. Cement and Concrete Composites 90, 150-160.
807 Niu, D., Li, D., Fu, Q., 2020. A 3D-IFU model for characterising the pore structure of
808 hybrid fibre-reinforced concrete. Materials & Design 188, 108473.
809 Pan, B., 2018. Digital image correlation for surface deformation measurement: historical
810 developments, recent advances and future goals. Measurement Science and Technology
811 29, 082001.
812 Pandit, A. V., Ranade, V. V., 2016. Chord length distribution to particle size distribution
813 62, 4215-4228.
814 Perre, P., Nguyen, D. M., Almeida, G., 2022. A macroscopic Washburn approach of liquid
815 imbibition in wood derived from X-ray tomography observations. Scientific Reports 12,
816 1750.
817 Perré, P., Nguyen, D. M., Almeida, G., 2022. A macroscopic Washburn approach of liquid
818 imbibition in wood derived from X-ray tomography observations. Scientific Reports 12,
819 1750.
820 Pham, C. T., Nguyen, B. T., Phan, H. T. Q., Pham, L. H., Hoang, C. N., Nguyen, N. N.,
821 Lee, P.-C., Kang, S.-J., Kim, J., Hoang, D., 2020a. Highly efficient fire retardant behavior,
822 thermal stability, and physicomechanical properties of rigid polyurethane foam based on
823 recycled poly(ethylene terephthalate). Journal of Applied Polymer Science 137, 49110.

Pham, L., Lin, X., Gravina, R. J., Tran, P., 2021. Influence of PVA and PP Fibres at Different Volume Fractions on Mechanical Properties of 3D Printed Concrete. pp. 2013-2024.
Pham, L., Tran, P., Sanjayan, J., 2020b. Steel fibres reinforced 3D printed concrete: Influence of fibre sizes on mechanical performance. Construction and Building Materials 250, 118785.
Picazo, A., Gálvez, J. C., Alberti, M. G., Enfedaque, A., 2018. Assessment of the shear behaviour of polyolefin fibre reinforced concrete and verification by means of digital image correlation. Construction and Building Materials 181, 565-578.
Promis, G., Douzane, O., Tran Le, A. D., Langlet, T., 2018. Moisture hysteresis influence on mass transfer through bio-based building materials in dynamic state. Energy and Buildings 166, 450-459.
Promis, G., Freitas Dutra, L., Douzane, O., Tran Le, A. D., Langlet, T., 2019. Temperature-dependent sorption models for mass transfer throughout bio-based building materials. Construction and Building Materials 197, 513-525.
Qin, Y., Wu, H., Zheng, Y., Wang, W., Yi, Z., 2019. Microscopic Texture of Polypropylene Fiber-Reinforced Concrete with X-Ray Computed Tomography. Advances in Civil Engineering 2019, 2386590.
Radojičić, V., Radulović, R., Tarić, M., Jović, S., 2022. The influence of the steel fibers on improvement of mechanical characteristic of concrete. Mechanics Based Design of Structures and Machines 50, 2929-2939.
Rahim, M., Douzane, O., Tran Le, A. D., Promis, G., Langlet, T., 2017. Experimental investigation of hygrothermal behavior of two bio-based building envelopes. Energy and Buildings 139, 608-615.
Raju, R. A., Lim, S., Akiyama, M., Kageyama, T., 2020. Effects of concrete flow on the distribution and orientation of fibers and flexural behavior of steel fiber-reinforced self-compacting concrete beams. Construction and Building Materials 262, 119963.
Ríos, J. D., Leiva, C., Ariza, M. P., Seitl, S., Cifuentes, H., 2019. Analysis of the tensile fracture properties of ultra-high-strength fiber-reinforced concrete with different types of steel fibers by X-ray tomography. Materials & Design 165, 107582.
Roostaei, M., Soroush, M., Hosseini, S. A., Velayati, A., Alkouh, A., Mahmoudi, M., Ghalambor, A., Fattahpour, V., 2020. Comparison of Various Particle Size Distribution Measurement Methods: Role of Particle Shape Descriptors. SPE International Conference and Exhibition on Formation Damage Control.
Rucka, M., Wojtczak, E., Knak, M., Kurpińska, M., 2021. Characterization of fracture process in polyolefin fibre-reinforced concrete using ultrasonic waves and digital image correlation. Construction and Building Materials 280, 122522.
Safari, H., Balcom, B. J., Afrough, A., 2021. Characterization of pore and grain size distributions in porous geological samples – An image processing workflow. Computers & Geosciences 156, 104895.

Schleiting, M., Wetzel, A., Krooß, P., Thiemicke, J., Niendorf, T., Middendorf, B., Fehling, E., 2020. Functional microfibre reinforced ultra-high performance concrete (FMF-UHPC). Cement and Concrete Research 130, 105993.
Segura-Castillo, L., Cavalaro, S. H. P., Goodier, C., Aguado, A., Austin, S., 2018. Fibre distribution and tensile response anisotropy in sprayed fibre reinforced concrete. Materials and Structures 51, 29.
Shanti, N. O., Chan, V. W. L., Stock, S. R., De Carlo, F., Thornton, K., Faber, K. T., 2014. X-ray micro-computed tomography and tortuosity calculations of percolating pore networks. Acta Materialia 71, 126-135.
Simões, T., Costa, H., Dias-da-Costa, D., Júlio, E., 2017. Influence of fibres on the mechanical behaviour of fibre reinforced concrete matrixes. Construction and Building Materials 137, 548-556.
Song, S.-B., Liu, J.-F., Yang, D.-S., Ni, H.-Y., Huang, B.-X., Zhang, K., Mao, X.-B., 2019a. Pore structure characterization and permeability prediction of coal samples based on SEM images. Journal of Natural Gas Science and Engineering 67, 160-171.
Song, S., Ding, Q., Wei, J., 2019b. Improved algorithm for estimating pore size distribution from pore space images of porous media. Physical Review E 100, 053314.
Sutton, M. A., Hild, F., 2015. Recent Advances and Perspectives in Digital Image Correlation. Experimental Mechanics 55, 1-8.
Thybring, E. E., Fredriksson, M., Zelinka, S. L., Glass, S. V., 2022. Water in Wood: A Review of Current Understanding and Knowledge Gaps 13, 2051.
Trofimov, A., Mishurova, T., Lanzoni, L., Radi, E., Bruno, G., Sevostianov, I., 2018. Microstructural analysis and mechanical properties of concrete reinforced with polymer short fibers. International Journal of Engineering Science 133, 210-218.
Tudisco, E., Andò, E., Cailletaud, R., Hall, S., 2017. TomoWarp2: A local digital volume correlation code. SoftwareX 6, 267-270.
Vicente, M. A., González, D. C., Mínguez, J., Tarifa, M. A., Ruiz, G., Hindi, R., 2018. Influence of the pore morphology of high strength concrete on its fatigue life. International Journal of Fatigue 112, 106-116.
Wen, F., Fan, H., Zhai, S., Zhang, K., Liu, F., 2020. Pore characteristics analysis and numerical seepage simulation of antifreeze permeable concrete. Construction and Building Materials 255, 119310.
Wu, M., Wu, J., Wu, J., Hu, B. X., 2018. A three-dimensional model for quantification of the representative elementary volume of tortuosity in granular porous media. Journal of Hydrology 557, 128-136.
Wu, Y., Tahmasebi, P., Lin, C., Zahid, M. A., Dong, C., Golab, A. N., Ren, L., 2019. A comprehensive study on geometric, topological and fractal characterizations of pore systems in low-permeability reservoirs based on SEM, MICP, NMR, and X-ray CT experiments. Marine and Petroleum Geology 103, 12-28.
Yu, F., Sun, D., Hu, M., Wang, J., 2019. Study on the pores characteristics and permeability simulation of pervious concrete based on 2D/3D CT images. Construction and Building Materials 200, 687-702.

Yuan, J., Wu, Y., Zhang, J., 2018. Characterization of air voids and frost resistance of concrete based on industrial computerized tomographical technology. Construction and Building Materials 168, 975-983.
Zhang, J., Ma, G., Ming, R., Cui, X., Li, L., Xu, H., 2018. Numerical study on seepage flow in pervious concrete based on 3D CT imaging. Construction and Building Materials 161, 468-478.
Zhang, P., Liu, G., Pang, C., Yan, X., Qin, H., 2017. Influence of pore structures on the frost resistance of concrete 69, 271-279.
Zhao, Z., Zhou, X.-P., 2019. An integrated method for 3D reconstruction model of porous geomaterials through 2D CT images. Computers & Geosciences 123, 83-94.
Zhao, Z., Zhou, X.-P., 2022. Pore-scale diffusivity and permeability evaluations in porous geomaterials using multi-types pore-structure analysis and X-μCT imaging. Journal of Hydrology 615, 128704.
Zhou, M., Caré, S., Courtier-Murias, D., Faure, P., Rodts, S., Coussot, P., 2018. Magnetic resonance imaging evidences of the impact of water sorption on hardwood capillary imbibition dynamics. Wood Science and Technology 52.
Zhou, M., Caré, S., King, A., Courtier-Murias, D., Rodts, S., Gerber, G., Aimedieu, P., Bonnet, M., Bornert, M., Coussot, P., 2019. Wetting enhanced by water adsorption in hygroscopic plantlike materials. Physical Review Research 1, 033190.